Supporting Information for Basal plane activation of two-dimensional transition metal dichalcogenides via alloying for hydrogen evolution reaction: first-principles calculations and machine learning prediction

Yiqing Chen [1], Ying Zhao [1], Pengfei Ou [1,2]*, Jun Song [1]*

[1] Department of Mining and Materials Engineering, McGill University, 3610 University St, Montreal, QC H3A 0C5, Canada

[2] Department of Chemistry, Northwestern University, 2145 Sheridan Rd, Evanston, IL 60208, United States

Corresponding Author: * pengfei.ou@northwestern.edu (P.Ou); jun.song2@mcgill.ca (J. Song)

S1. Data distribution

To train the ML models, data sets for both ΔG_H and stability prediction were randomly split as training and testing sets according to a 7:3 ratio. For ΔG_H prediction model, as shown in **Fig. S1a**, ΔG_H distributions of the training and testing set have similar shapes, with data distributed in the range of (-0.5, 2.5) eV. Fig. **S2a** shows the distribution of data for stability prediction. Similarly, it is found that stability data are evenly distributed in both the training and testing set. The good distribution of data for both ΔG_H and stability prediction ensures the accuracy of the ML training process.

We also evaluated the distribution of alloy types for data sets from ΔG_H and stability prediction, as shown in **Fig. S1b** and **Fig. S2b**. The distribution plots suggest that the data we used for training ML are evenly distributed in different alloy types and can appropriately represent all 2D TMDC alloys.

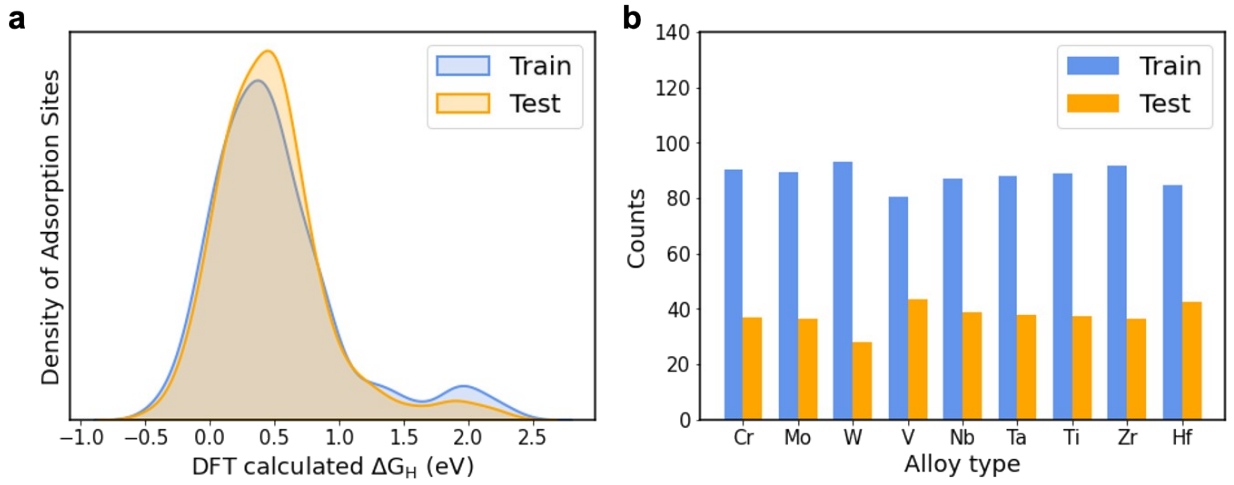

Fig. S1 a. The normalized distribution of the DFT-calculated ΔG_H for the training and testing set, respectively. **b.** The distribution of alloy types for the training and testing set for ΔG_H prediction.

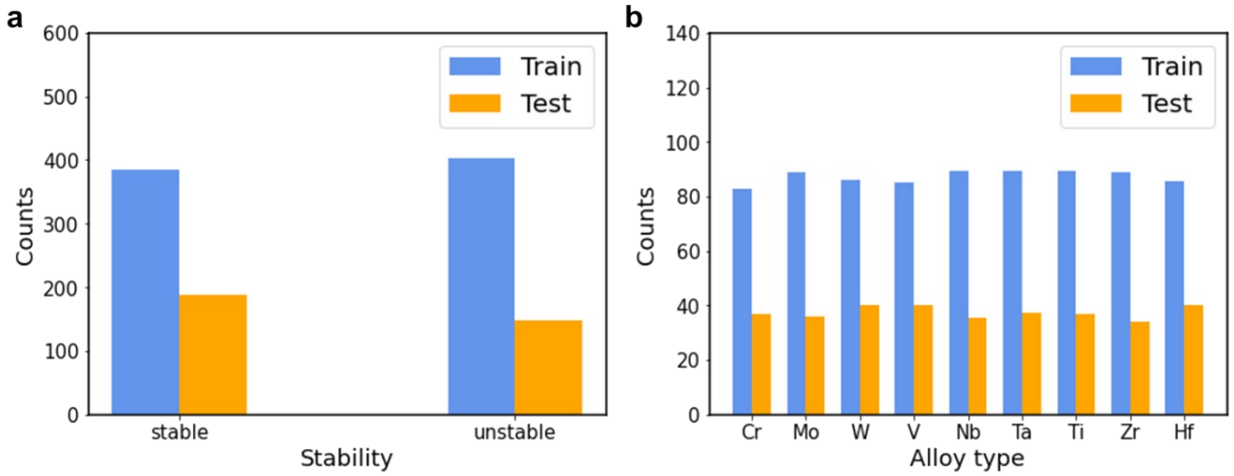

Fig. S2 a. The distribution of stability of alloys for the training and testing set. **b.** The distribution of alloy types for the training and testing set for stability prediction.

S2. Performance of ML model

To evaluate the performance of our ML models, in this study, we used mean absolute error (MAE) and root-mean-square error (RMSE) to measure the errors of the regression model, and accuracy and F1-score to measure the errors of the classification model.

MAE is defined as the sum of absolute values divided by the number of data:

$$MAE = \frac{1}{N}\sum_{i=1}^{N}|y - y_i| \tag{S1}$$

where N, y and y_i represent the number of data, observed value and predicted value.

RMSE is the standard deviation of the predicted errors calculated as:

$$RMSE = \left[\frac{1}{N}\sum_{i=1}^{N}(y - y_i)^2\right]^{1/2} \tag{S2}$$

Accuracy is the fraction of correct predictions:

$$Accuracy = \frac{Number\ of\ correct\ predictions}{Total\ number\ of\ predictions} \tag{S3}$$

And F1-score is defined as the harmonic mean of precision and recall:

$$F1 = \frac{2 * precision * recall}{precision + recall} \tag{S4}$$

where precision is the number of the true positives over the number of predicted positives, and recall is the number of true positives over the number of actual positives.

In this work, we used regression to predict ΔG_H and classification to predict the stability of the 2D TMDC alloys. 10-fold cross-validation was used when evaluating the ML models. The corresponding learning curves of these two models are presented in **Fig. S3**, which show the magnitude of the modeling error as the size of dataset varies. The convergence of the training and validation scores indicates that we have enough data used for training.

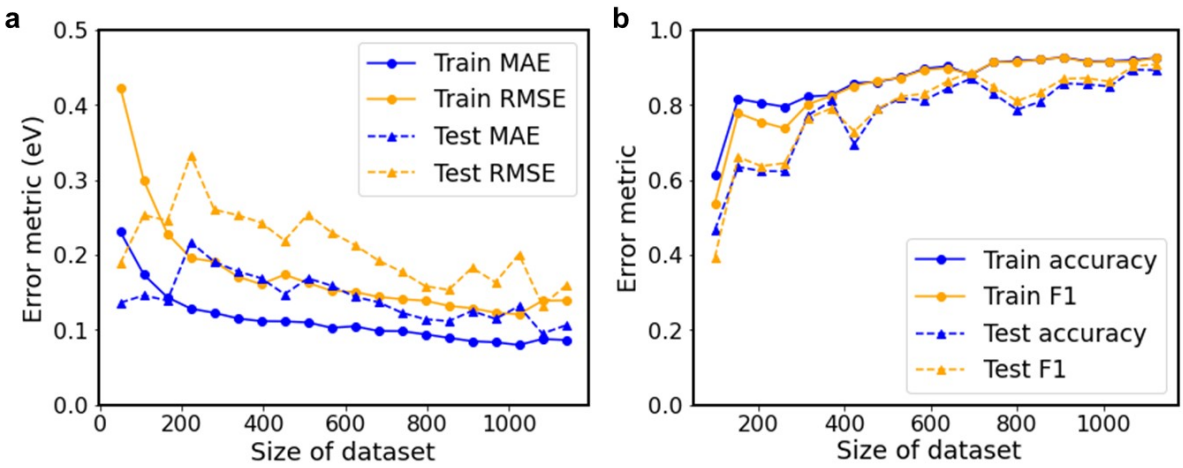

Fig. S3. Error metrics vs. size of dataset for the prediction of **a.** ΔG_H and **b.** stability of 2D TMDC alloys.

S3. Gibbs free energies of hydrogen adsorption on pristine MX_2

Table S1. Gibbs free energies of hydrogen adsorption on pristine MX_2

MS_2	$\Delta G_{H\text{-}MS2}$ (eV)	MSe_2	$\Delta G_{H\text{-}MSe2}$ (eV)
CrS_2	1.37	$CrSe_2$	1.39
MoS_2	2.00	$MoSe_2$	2.16
WS_2	2.25	WSe_2	2.28
VS_2	0.28	VSe_2	0.69
NbS_2	-0.01	$NbSe_2$	0.36
TaS_2	0.17	$TaSe_2$	0.46
TiS_2	0.04	$TiSe_2$	0.48
ZrS_2	0.126	$ZrSe_2$	0.540
HfS_2	0.347	$HfSe_2$	0.671

S4. Feature vector assignment

Fig. S4 illustrates how a feature vector is assigned to each unique alloy structure. Here, we use $Mo_{0.89}W_{0.11}S_2$ as a representative. Transition metal sites in the supercell are numbered and each site is described in order by the following three properties: the atomic number of the element (Z), the Pauling electronegativity of the element (χ), and the Gibbs free energy of hydrogen adsorption of pristine MX_2 ($\Delta G_{H\text{-}MX2}$) for ΔG_H prediction or total energy of pristine MX_2 (E_{MX2}) for stability prediction. After describing all transition metal sites, Z and χ of the chalcogen atom are appended at the end of the feature vector. A 29-dimension vector is created and can represent each alloy configuration in our study.

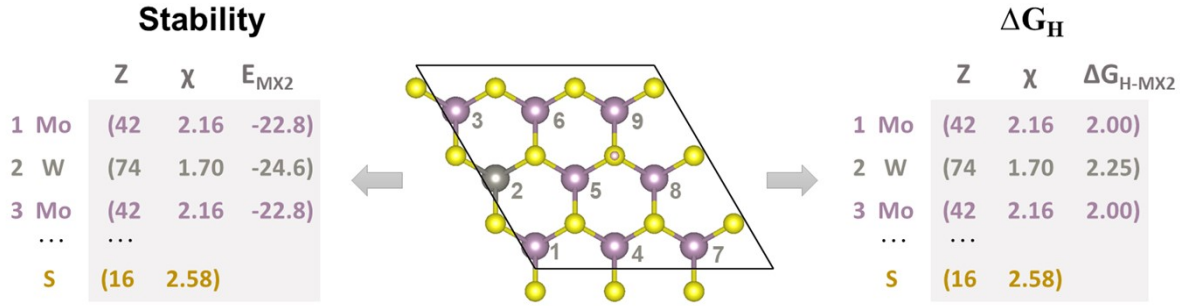

Fig. S4. Illustration of feature vector assignment. Alloy structures are reduced to numerical representations.

S5. Electrocatalytic Activity of 72 TMDC Alloys

Fig. S5-10 show the machine learning predicted ΔG_H values for various TMDC ternary alloys at different concentrations.

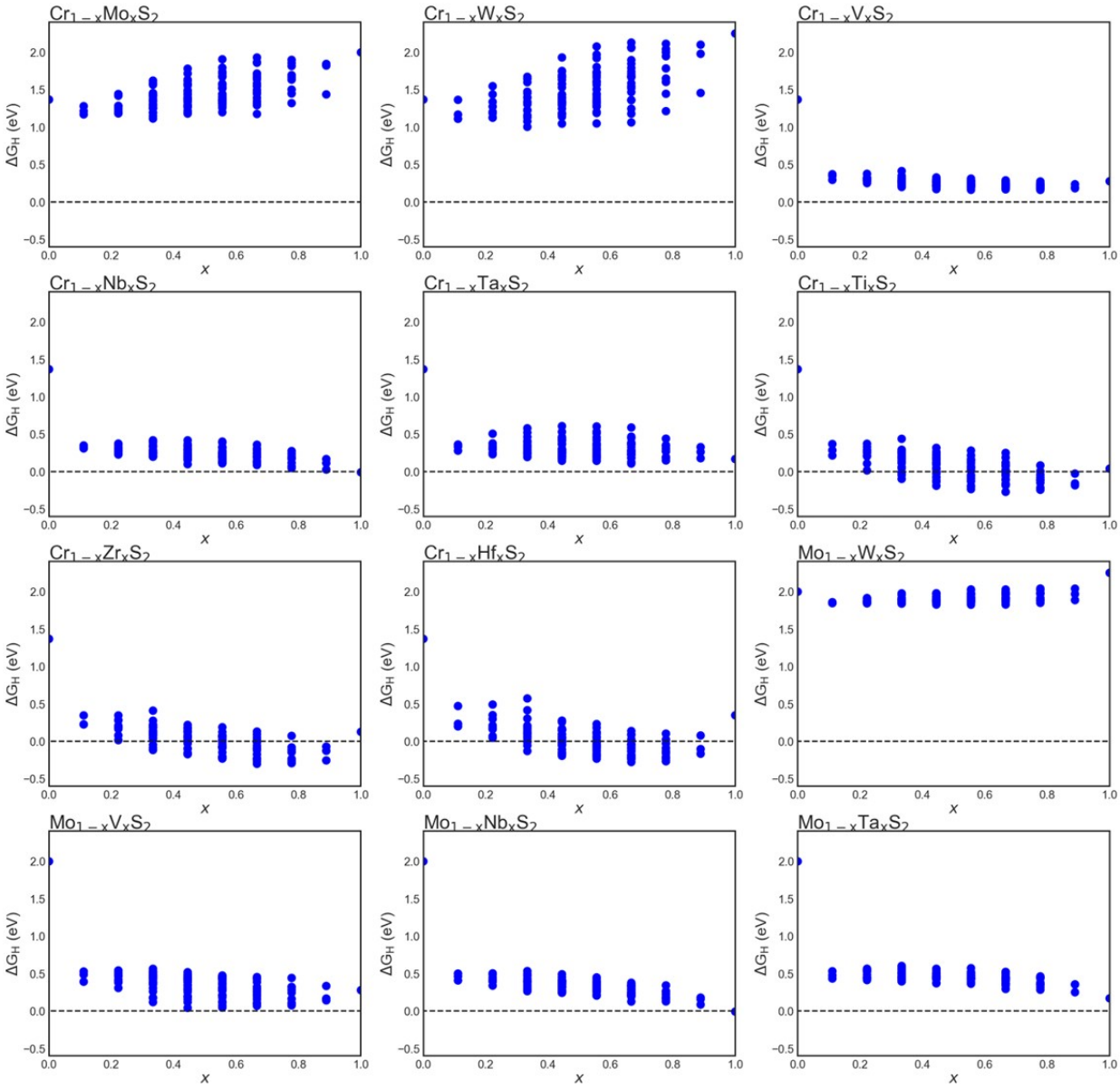

Fig. S5. Machine learning predicted ΔG_H values of TMDC ternary alloys at different concentrations. Black dash lines indicate the optimal ΔG_H desirable for HER.

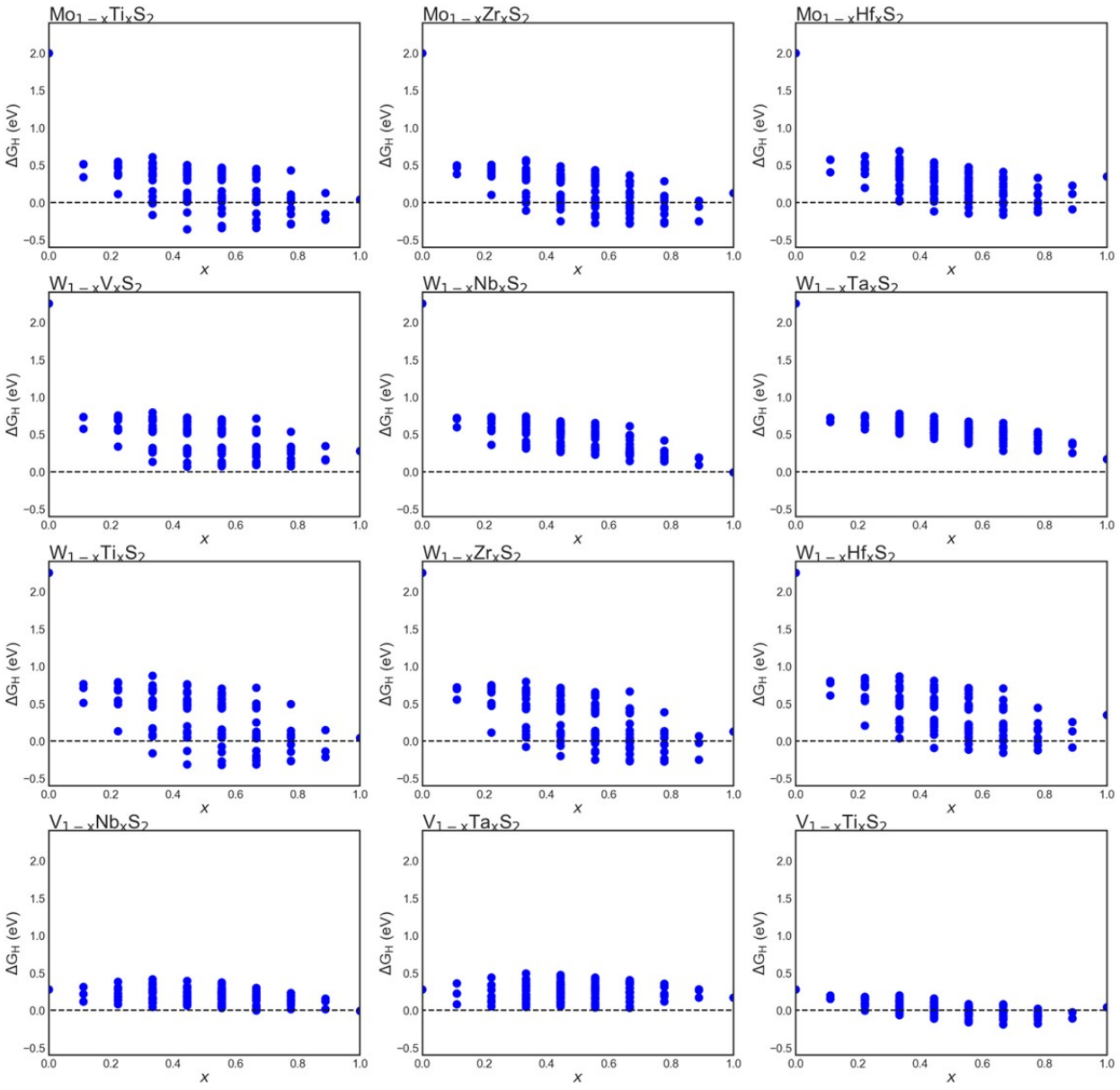

Fig. S6. Machine learning predicted ΔG_H values of TMDC ternary alloys at different concentrations. Black dash lines indicate the optimal ΔG_H desirable for HER.

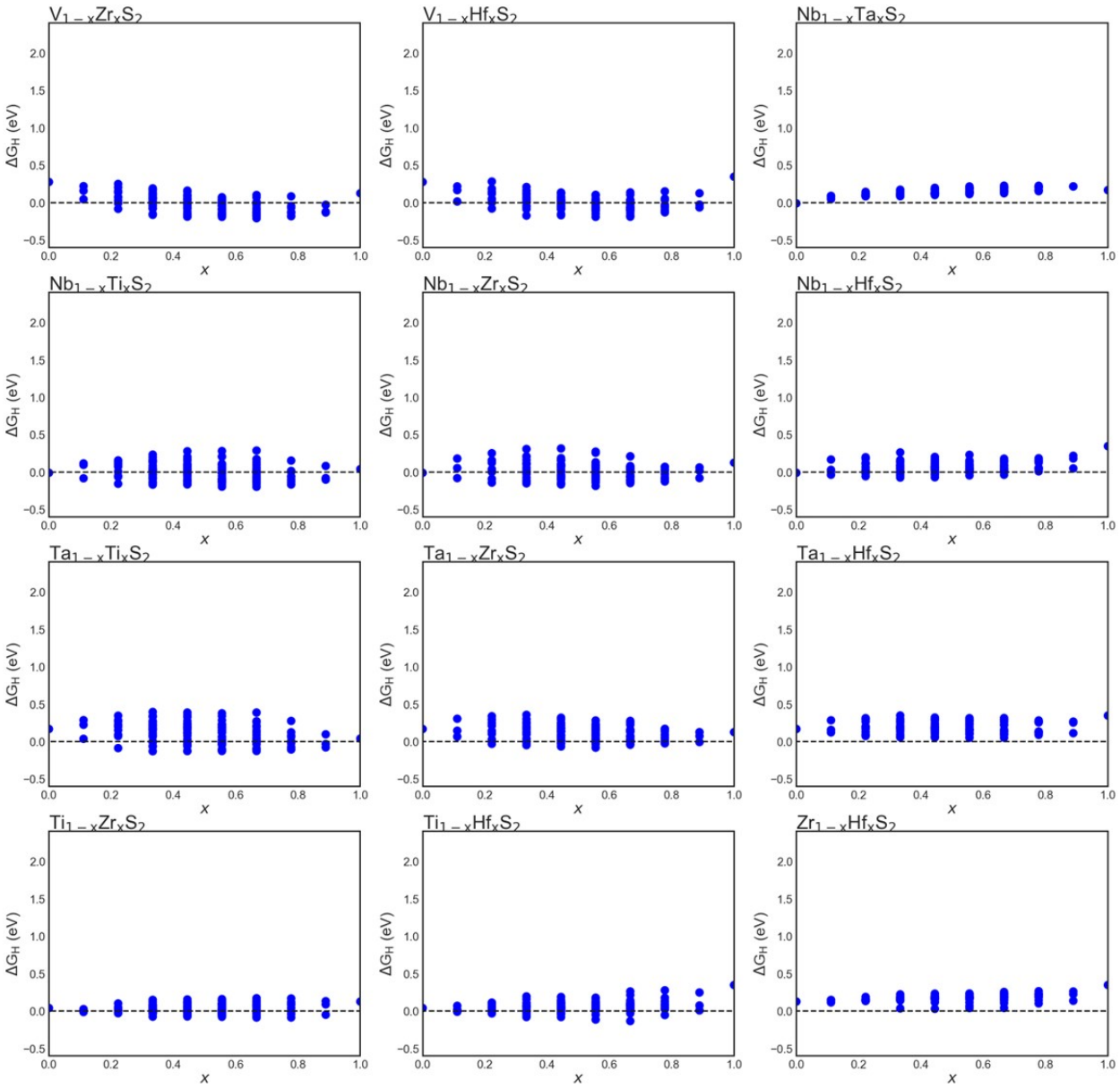

Fig. S7. Machine learning predicted ΔG_H values of TMDC ternary alloys at different concentrations. Black dash lines indicate the optimal ΔG_H desirable for HER.

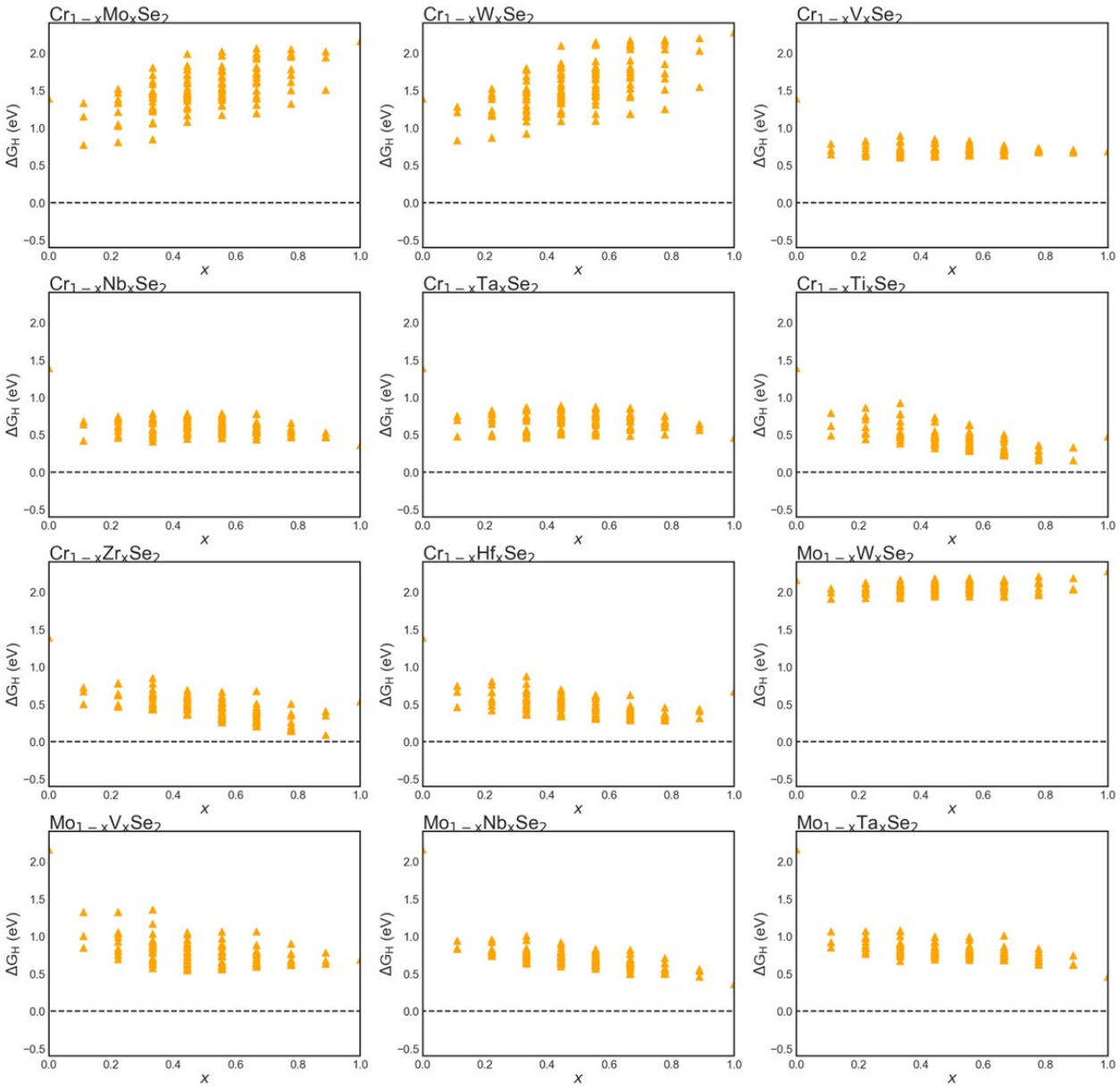

Fig. S8. Machine learning predicted ΔG_H values of TMDC ternary alloys at different concentrations. Black dash lines indicate the optimal ΔG_H desirable for HER.

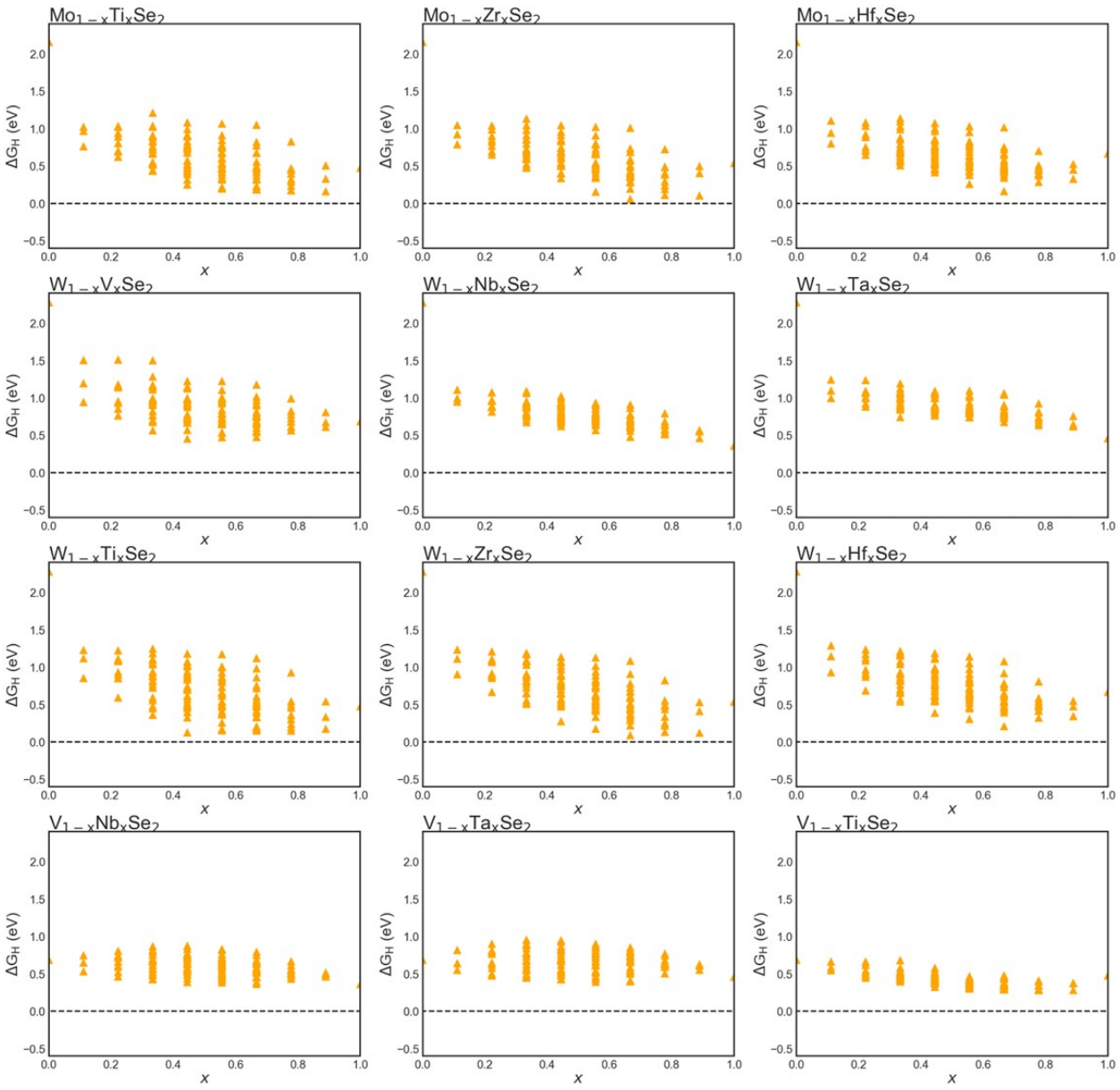

Fig. S9. Machine learning predicted ΔG_H values of TMDC ternary alloys at different concentrations. Black dash lines indicate the optimal ΔG_H desirable for HER.

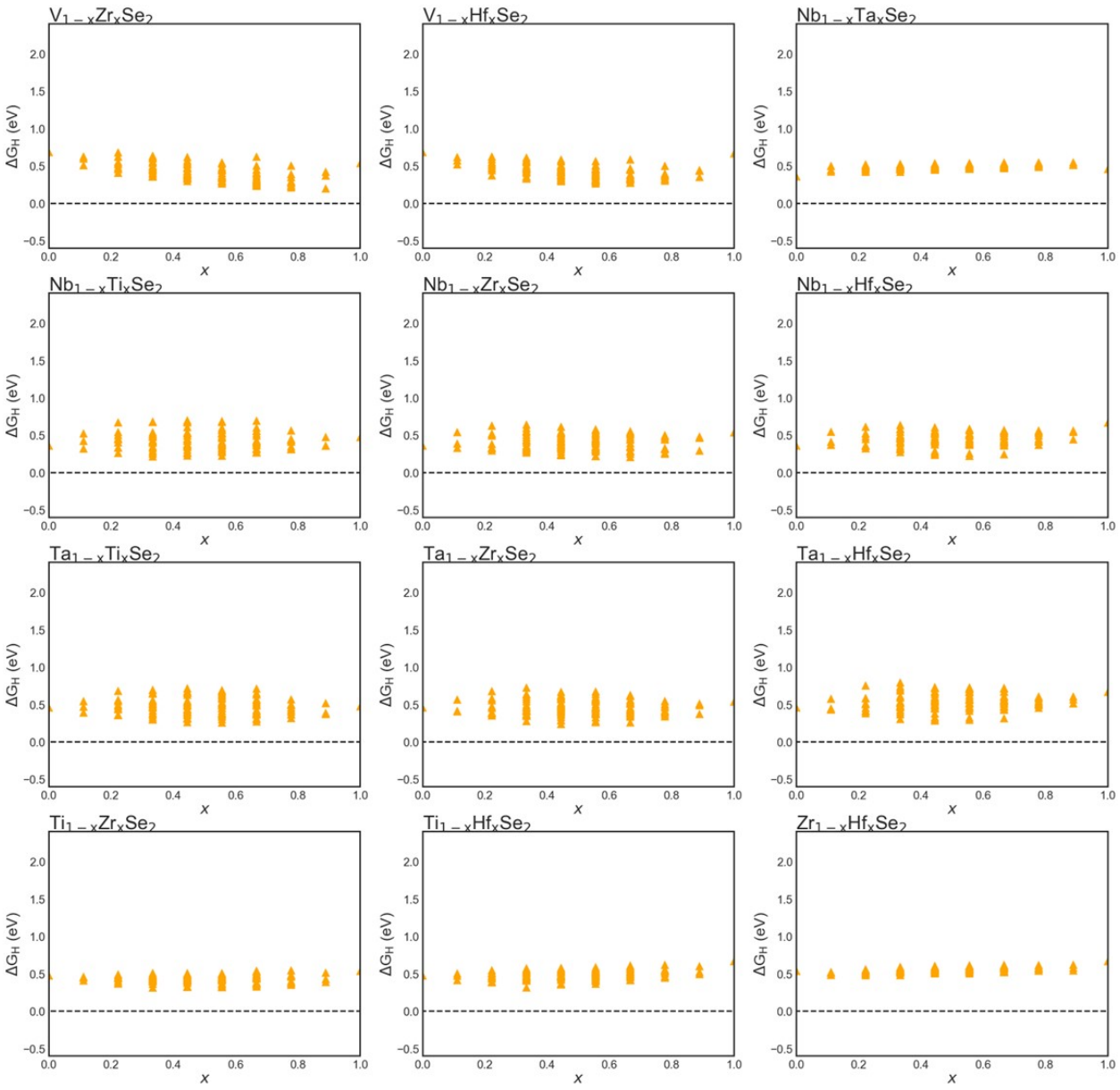

Fig. S10. Machine learning predicted ΔG_H values of TMDC ternary alloys at different concentrations. Black dash lines indicate the optimal ΔG_H desirable for HER.

S6. HER activity mapping for MSe_2

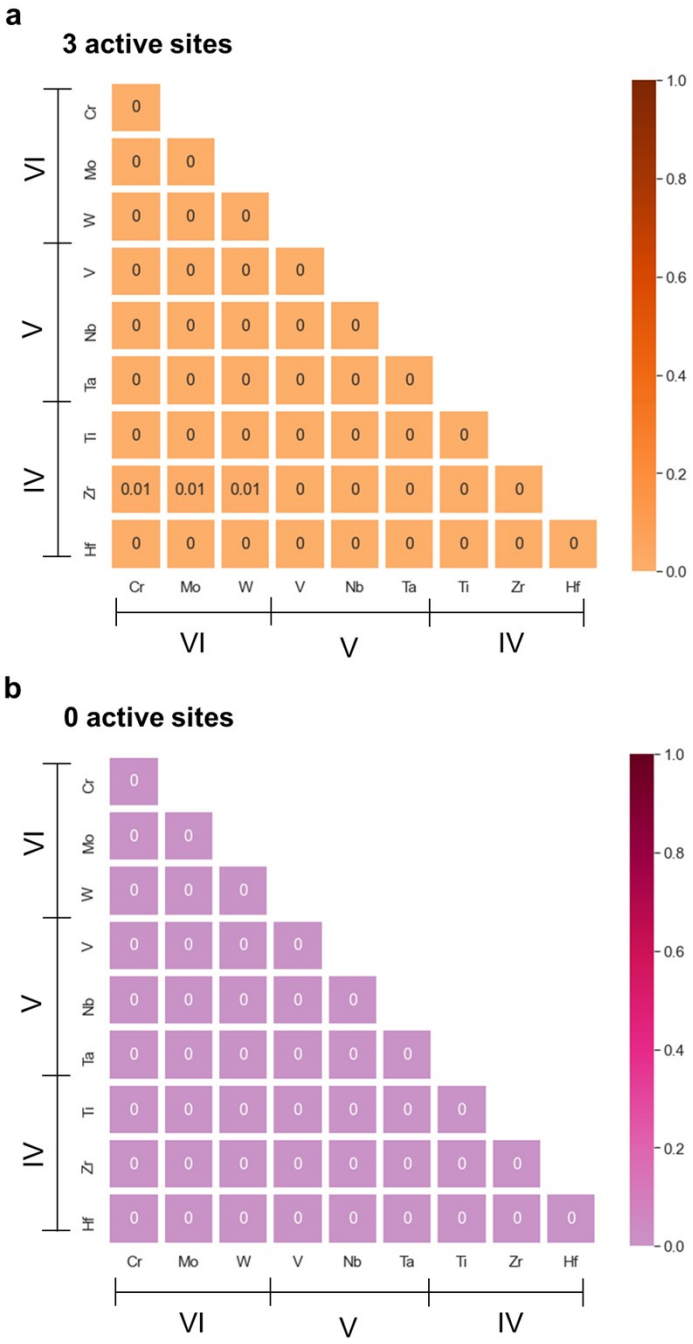

Fig. S11 HER activity heatmaps for MSe_2 alloys showing **a.** the fraction of adsorption sites of ΔG_H within the optimal range of (-0.1, 0.1) eV for each alloy, and **b.** the fraction of adsorption sites that are stable and have optimal ΔG_H for each MSe_2 alloy. The number indicates the fraction value an alloy exhibits, which is also reflected by the color.

S7. HER activity mapping for MS_2 at different concentrations

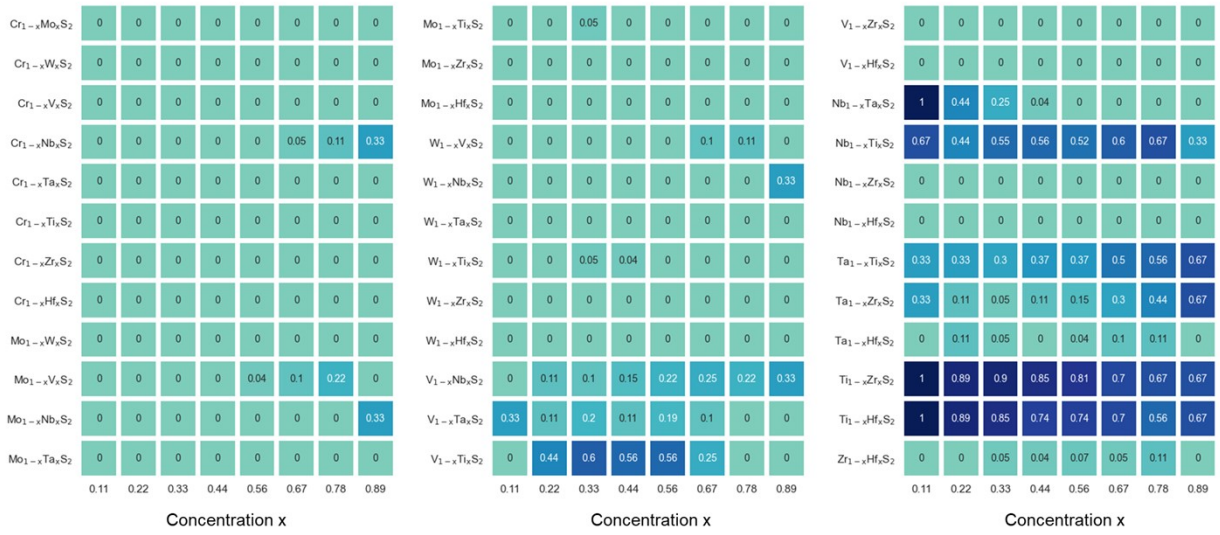

Fig. S12 HER activity heatmap for MS_2 alloys showing the fraction of adsorption sites that are stable and have optimal ΔG_H for each alloy at different concentrations. The number indicates the fraction value an alloy exhibits, which is also reflected by the color.

S8. The effect of configuration changes

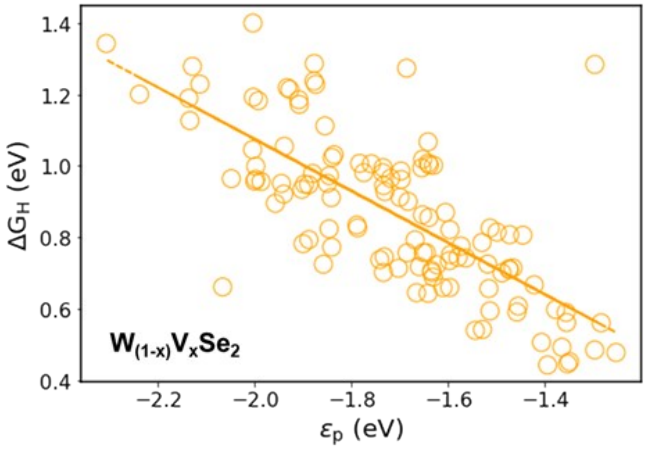

Fig. S13 Relationship between ε_p values and ΔG_H for $W_{(1-x)}V_xSe_2$ alloys with different configurations.

S9. p-band center ε_p vs. concentration x of TMDC alloys

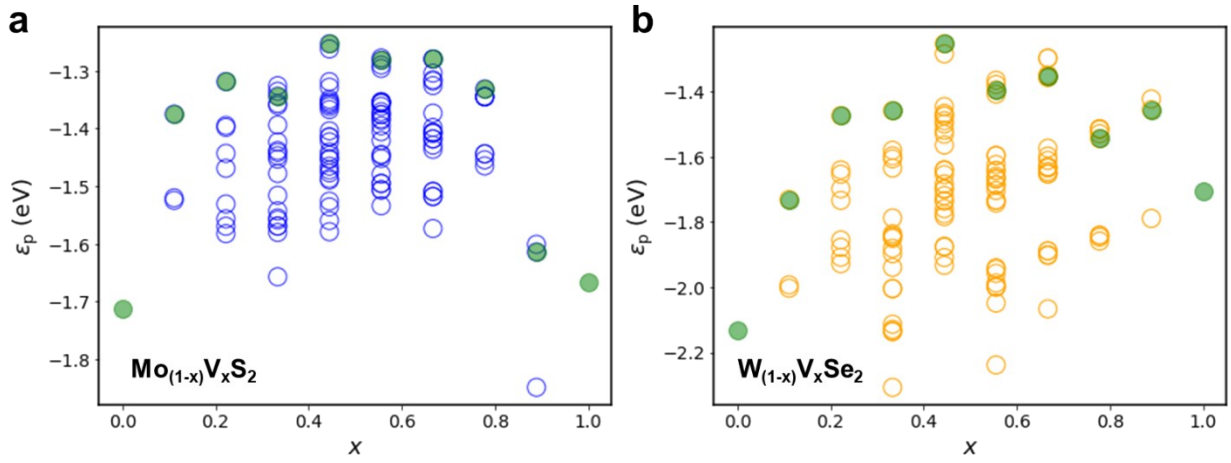

Fig. S14 p-band center ε_p vs. concentration x plots for all adsorption sites in $Mo_{(1-x)}V_xS_2$ and $W_{(1-x)}V_xSe_2$. Green solid points here highlight the adsorption sites with the best (lowest) ΔG_H at each concentration.

S10. Charge transfer induced p-band center change $\Delta\varepsilon_{CEX}$ vs. concentration *x* of TMDC alloys

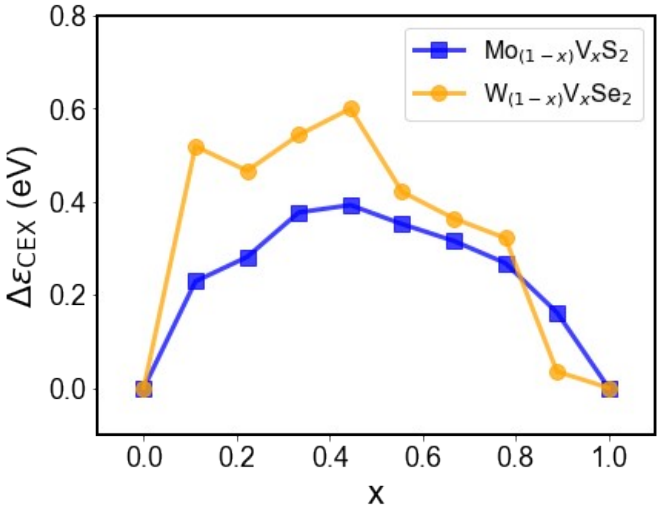

Fig. S15 The change of p-band center during the charge transfer step $\Delta\varepsilon_{CEX}$ of the adsorption sites in $Mo_{(1-x)}V_xS_2$ and $W_{(1-x)}V_xSe_2$ alloys with the best (lowest) ΔG_H as a function of the composition x.

S11. Example adsorption configurations

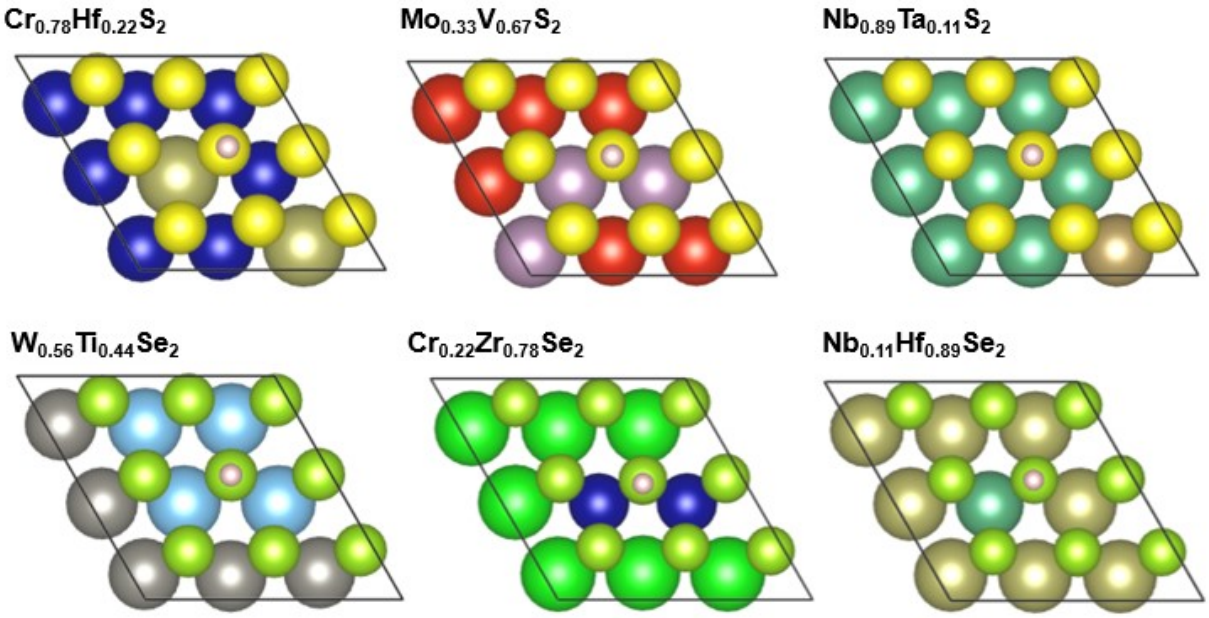

Fig. S16. Example hydrogen adsorption configurations on six representative TMDC alloys, where S atoms, Se atoms and H atoms are colored yellow, green, and pink respectively.